Article

Preferential Oxidation of CO over CoFe₂O₄ and M/CoFe₂O₄ (M = Ce, Co, Cu or Zr) Catalysts

Mehdi Béjaoui [1], Abdelhakim Elmhamdi [1], Laura Pascual [2], Patricia Pérez-Bailac [2], Kais Nahdi [1] and Arturo Martínez-Arias [2,*]

1   Laboratoire d'Application de la Chimie aux Ressources et Substances Naturelles et à l'Environnement, Faculté des Sciences de Bizerte, Université de Carthage, 7021 Zarzouna, Bizerte, Tunisia; bejaoui.mehdi@yahoo.fr (M.B.); elmhamdi.abdelhakim@gmail.com (A.E.); nahdi.kais@gmail.com (K.N.)
2   Instituto de Catálisis y Petroleoquímica, CSIC, Campus de Cantoblanco, C/Marie Curie 2, 28049 Madrid, Spain; laura.pascual@icp.csic.es (L.P.); patricia.perez@csic.es (P.P.-B.)
*   Correspondence: amartinez@icp.csic.es; Tel.: +34-915854940

Abstract: CoFe₂O₄ prepared by sol-gel has been examined with respect to its catalytic performance for preferential CO oxidation in a H₂-rich stream. In turn, the promoting effects of incorporation of Ce, Co, Cu, and Zr by impregnation on the surface of CoFe₂O₄ on the process are examined as well. The catalysts have been characterized by N₂ adsorption, X-ray diffraction (XRD), high resolution transmission electron microscopy (HRTEM), temperature programmed reduction (TPR), and X-ray photoelectron spectra (XPS), as well as diffuse reflectance infrared DRIFTS under reaction conditions with the aim of establishing structure/activity relationships for the mentioned catalyst/process. It is shown that while the presence of the various metals on CoFe₂O₄ hinders a low temperature CO oxidation process, it appreciably enhances the activity above 125 °C. This is basically attributed to the surface modifications, i.e. cobalt oxidation, induced in CoFe₂O₄ upon introduction of the metals. In turn, no methanation activity is observed in any case except for the copper-containing catalyst, in which achievement of reduced states of cobalt appears most favored.

Keywords: CoFe₂O₄ spinel; supported Co; Ce; Zr and Cu; XRD; TEM; TPR; XPS fitting; CO-PROX; DRIFTS

1. Introduction

During the last years, the global consumption of fossil fuels has increased markedly, leading to environmental problems. Therefore, the development of new green resources is currently one of the most important and relevant research topics [1,2]. Fuel cell power generation is considered as the most efficient energy technology to produce electricity from chemical fuels [2]. Among the various types of fuel cells, proton exchange membrane fuel cells (PEMFC), which combine high power density, efficiency, and environmental friendliness, represent the most interesting ones for power generation, particularly for mobile applications [2,3]. The primary fuel for PEMFC is hydrogen. Hydrogen can be produced by a number of different processes, but natural gas reforming is by far the dominant technology for production in commercial quantities, while the reforming of hydrocarbons or oxygenated hydrocarbons is also considered most practical for on-board hydrogen production [4,5]. The PEMFC operation requires the use of high-purity hydrogen and, for that purpose, the reforming reaction is sequentially followed by the water-gas shift (WGS) and CO preferential oxidation (CO-PROX) catalytic reactions [4,5]. The latter reaction focuses on the elimination of CO, which is known to deactivate Pt-based electrocatalysts typically employed in PEMFC. The CO-PROX reaction is considered the most effective and economical method to reduce the CO levels to acceptable concentrations [4–7]. Ideally, CO-PROX catalysts should work at relatively low temperatures (close to that of PEMFC operation), have high CO oxidation activity, and be selective towards CO₂ instead of H₂O

(or other products like methane, for instance) [8]. Some noble metals and transition-metal oxides are efficient for the CO-PROX reaction, and the latter, despite their lower general robustness, are mostly preferred mainly for economic reasons [8]. Among these, cobalt-based spinel oxide nanoparticles can be an interesting alternative, taking into account their high activity for CO oxidation [9,10]. This has been related to the particularly high activity of cobalt in the spinel octahedral site, while cobalt in the tetrahedral site appears much less active [9,10].

The cobalt ferrite ($CoFe_2O_4$) presents the inverse (or partially inverse) spinel structure in which an important part of the Co^{2+} cations are located in the octahedral sites and corresponding part of Fe^{3+} cations are tetrahedrally coordinated [11,12]. Such structure is proposed to provide a good level of CO oxidation activity to the ferrite, attributed to the formation of very active octahedral Co^{3+} upon oxidation under the reactant stream [9], with respect to other analogous cobalt spinel formulations with the normal spinel structure [9,10,13–16]. Few reports in the literature have studied cobalt ferrite-based catalysts for the CO-PROX process [17,18]. Chagas et al. have examined cobalt ferrite nanoparticles prepared through the glucose-assisted hydrothermal method [17]. Their results show that the material exhibits high CO conversion and good stability on stream at 250 °C. However, the presence of CO_2 and H_2O affect the CO conversion and might inhibit the reaction kinetics for concentrations above the feed level, although it has no influence on the chemical structure of the surface-active sites. In turn, the work by Qwabe et al. examined Co–Fe mixed metal oxide catalysts prepared from hydrotalcite precursors and in which $CoFe_2O_4$ constitutes the main active component [18]. They appear able to operate at 100% CO conversion between 120 and 180 °C and show good stability although, as mentioned for the catalyst examined by Chagas et al. [17], a deactivation by CO_2 or H_2O presence in the feed stream was also detected [18].

In this context, the present work explores the CO-PROX properties of a $CoFe_2O_4$ catalyst prepared by sol-gel, a method which enables the development of a crystalline, homogeneous, and high purity material [19]. Additionally, copper, cobalt, cerium, and zirconium are incorporated to the surface of $CoFe_2O_4$ in order to examine possible promoting effects for the process. Recently, Chen et al. have used chemical co-precipitation and wet impregnation methods to synthesize different catalysts of copper supported on $CoFe_2O_4$ [20]. An enhanced catalytic activity for CO oxidation is observed upon copper incorporation to the catalyst. It is attributed to the presence of more surface-active oxygen species and oxygen vacancies, which can enhance the adsorption of CO on Cu^+ species and the O_2 activation on oxygen vacancies. In turn, oxidized states of cobalt at the surface can also enhance the CO oxidation activity of the catalyst [9]. Cerium oxide can be also a promoter of the CO oxidation activity as well as it can provide more resistance to the presence of water in the reactant mixture according to results observed in systems in which it was combined with other spinel oxides or cobalt oxide [21,22]. In turn, zirconium has been also explored as promoter and in order to compare also with cerium oxide as known good oxygen transport material (in the form of oxide), but without intrinsic redox activity. On this basis, the systems were explored in a multi-technique analysis (X-ray diffractometry (XRD), N_2 adsorption at −196 °C, high resolution transmission electron microscopy (HRTEM), X-ray photoelectron spectra (XPS), temperature programmed reduction (TPR)) for catalyst characterization while the catalytic activity CO-PROX tests have been complemented by operando-DRIFTS spectroscopy under reaction conditions with the aim of establishing on the whole structure/activity relationships for this type of catalyst/process.

2. Results and Discussion

2.1. Characterization

Basic textural properties of the samples, extracted from corresponding N_2 adsorption/desorption isotherms (collected in Supporting Information), are summarized in Table 1. The samples exhibit type IV isotherms with a hysteresis loop at a relative pressure >0.5, indicating the mesoporous structure of the materials. $CoFe_2O_4$ exhibits the highest specific

surface area (36.8 $m^2 g^{-1}$). With the presence of the different promoters at 1 wt.% loading, the surface area of the catalysts decreases, to a different extent depending on the nature of the promoter, which must be attributed to the clogging of support pores with the different promoter oxides. The same trend is also observed in the pore volume estimations. The increase produced in S_{BET} for 10Ce/CoFe with respect to 1Ce/CoFe must be related to the formation of a new porous structure related to the ceria component. A similar result has been observed previously for $CuMn_2O_4$-supported CeO_2 in which such an increase was observed to be produced above monolayer coverage with ceria [21], consistent with observation for 10Ce/CoFe.

Table 1. Basic textural properties for the indicated catalysts.

Catalyst	S_{BET} ($m^2 g^{-1}$)	Pore volume ($cm^3 g^{-1}$)	Average Pore Size (nm)
$CoFe_2O_4$	36.8	0.235	26.0
1Cu/CoFe	27.9	0.127	17.9
1Co/CoFe	27.8	0.154	20.9
1Ce/CoFe	30.1	0.156	21.2
10Ce/CoFe	35.7	0.128	15.2
1Zr/CoFe	36.1	0.219	23.8

The XRD patterns for all the catalysts are shown in Figure 1. Peaks centered at $2\theta \sim 18.4°$, $30.2°$, $35.6°$, $37.1°$, $43.2°$, $53.6°$, $57.2°$, $62.8°$, and $74.3°$ are observed in all cases, which can be assigned as the Bragg planes (111), (220), (311), (222), (400), (422), (511 or 333), (440), and (533), respectively, of the cubic crystalline structure (space group Fd3m) of spinel $CoFe_2O_4$ with crystals of about 18 nm (somewhat smaller for sample $CoFe_2O_4$ than for the modified samples, suggesting that the impregnation and further calcination of $CoFe_2O_4$ favors some sintering or crystallization in it), as determined with the Scherrer equation [11]. Additional features are only detected for 10Ce/CoFe, in which broad peaks are detected at ca. $29.0°$ and $47.7°$, which are related to most intense (111) and (220) peaks of the cubic fluorite CeO_2 structure [21]. The formation of CeO_2 crystals in this system is related to its relatively high cerium loading, corresponding to about 1.7 theoretical monolayers of CeO_2 [21], along with the saturation of the dispersion capability of the $CoFe_2O_4$ surface. In turn, the absence of features related to the added metals in the 1 wt.% samples can be related to the relatively low loading or to the achievement of a relatively high dispersion state over the surface of the $CoFe_2O_4$; further information in this sense is presented in the XPS results below.

The morphological/structural properties of representative catalysts of the series were complemented by HRTEM, as shown in Figure 2. The support $CoFe_2O_4$ consists of polyhedral (close to spherical) particles with a size around 20 nm (Figure 2b). The selected area electron diffraction pattern (SAED) displayed in the inset shows polycrystalline rings consistent with the spinel type structure (Fd3m) of the $CoFe_2O_4$ phase, in agreement with XRD analysis above. A detailed HRTEM micrograph and its corresponding FFT of one particle oriented along the [112] zone axis is displayed in Figure 2a. Representative HRTEM images of 1Ce/CoFe (Figure 2c,d), 1Co/CoFe (Figure 2e,f), and 1Cu/CoFe (Figure 2g,h) are also presented. In any case, the obtained results are similar to those observed for $CoFe_2O_4$, exhibiting the same (Fd3m) structure, which is also in agreement with XRD analysis. Sporadically, isolated CeO_2 particles of 5 nm can be found in some areas of 1Ce/CoFe. In Figure 2c, the HRTEM image shows a fluorite type CeO_2 particle oriented in the [100] zone axis over the spinel type along the same direction. Neither Co- nor Cu-containing additional phases were found in 1Co/CoFe or 1Cu/CoFe, evidencing a good dispersion level in any of the three cases. In this sense, X-ray energy-dispersive spectroscopy XEDS mapping of 1Cu/CoFe (shown in Supporting Information) shows that the dispersion of the Cu phase is very homogeneous over the $CoFe_2O_4$ support.
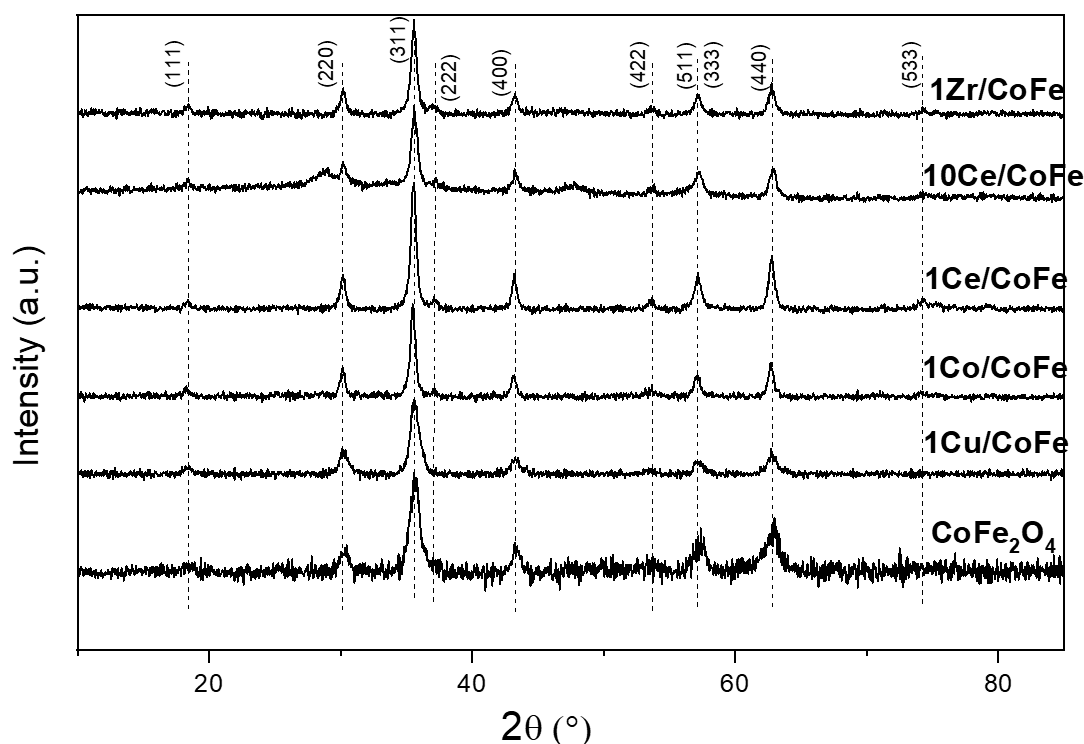
Figure 1. X-ray diffractograms of the indicated samples. Miller indexes for the $CoFe_2O_4$ phase are marked.
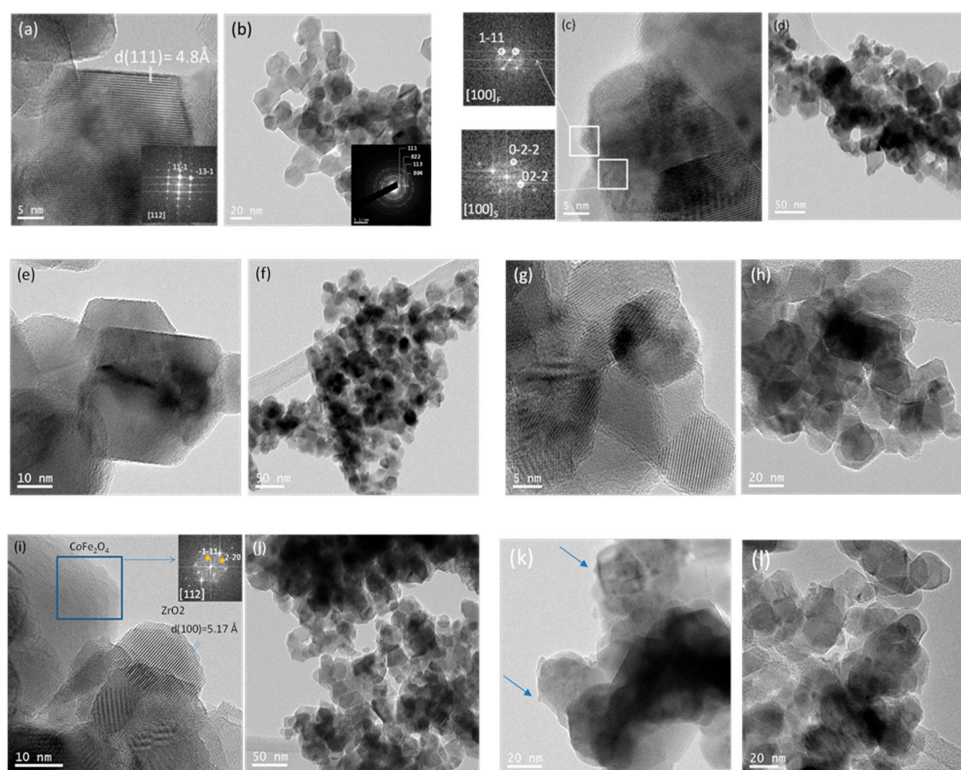

Figure 2. (**a**) HRTEM (high resolution transmission electron microscopy) of a particle of $CoFe_2O_4$ oriented down the [112] zone axis of the spinel structure. (**b**) Representative low magnification TEM micrograph of the $CoFe_2O_4$ and its corresponding SAED pattern. (**c**) HRTEM of the 1Ce/CoFe sample and the FFT of both phases (fluorite and spinel) oriented along the [100] zone axis in both structures. (**d**) TEM micrograph of the 1Ce/CoFe sample. (**e**) HRTEM of the 1Co/CoFe sample. (**f**) Low magnification TEM image of 1Co/CoFe. (**g**) HRTEM of the 1Cu/CoFe sample. (**h**) Low magnification TEM image of 1Cu/CoFe. (**i**) HRTEM of the 1Zr/CoFe sample. The FFT shows a spinel $CoFe_2O_4$ particle in the [112] zone axis. (**j**) Low magnification TEM image of 1Zr/CoFe. (**k**,**l**) TEM micrographs of the 10Ce/CoFe sample. Blue arrows mark dispersed CeO_2 particles.

In contrast, some relatively large zirconia crystals of ca. 15 nm are sporadically found over 1Zr/CoFe (Figure 2i,j) (evidenced by the presence of the interplanar distances of 5.17 Å corresponding with the d(100) of the ZrO_2 phase), suggesting a lower dispersion degree achieved in this case for the added metal, which can explain the relatively low specific area decrease observed for this catalyst in comparison with $CoFe_2O_4$ (Table 1); the absence of specific features related to zirconia in its X-ray diffractogram could be due to the relatively low metal loading. Nevertheless, for 10Ce/CoFe, the presence of small particles differentiated over the $CoFe_2O_4$ support, which may correspond to CeO_2 crystals in accordance with XRD (Figure 1), is evident in the TEM and HRTEM images of Figure 2k,l (as marked with arrows).

H_2-TPR experiments were performed in order to explore the redox properties of the catalysts, as shown in Figure 3. Plots are normalized by weight, and relative hydrogen consumptions are similar between them (a little lower for 10Ce/CoFe). For $CoFe_2O_4$, following a first weak peak between ca. 180–300 °C, three strong reduction peaks appear at around 350, 450, and 530 °C, respectively. These three peaks are characteristic for the reduction of $CoFe_2O_4$ and have been attributed to the reduction of the Co^{2+} to metallic cobalt (first one) and to the sequential, more or less promoted by the metallic cobalt [15,23], reduction of Fe^{3+} to metallic iron (the two ones at higher temperature) [20,24]. In turn, the weaker peak between ca. 180–300 °C can be due to the reduction of surface cobalt species [24]. On the other hand, the profiles of 1Ce/CoFe, 10Ce/CoFe, and 1Co/CoFe show important similarities with the profile observed for the bare $CoFe_2O_4$ support. The main differences are related to a shift to higher temperature of the peaks related to $CoFe_2O_4$ reduction, which evidences the higher difficulty for its reduction in the presence of the new components at their surface. In contrast, similar three peaks for the $CoFe_2O_4$ reduction appear strongly shifted to lower temperatures for 1Cu/CoFe. In addition, a peak at ca. 130 °C appears in this sample and is related with the reduction of copper species to metallic copper. This helps in hydrogen activation, thus promoting the reduction of the $CoFe_2O_4$ support. Note that in principle, dispersed cobalt species in the form of Co^{3+}, which could be present at the surface of 1Co/CoFe (*vide infra*), are expected to be reduced at temperatures in a similar range as those observed for $CoFe_2O_4$ which, in addition to the broadness of the observed features, complicates the analysis of differences between both samples [25].
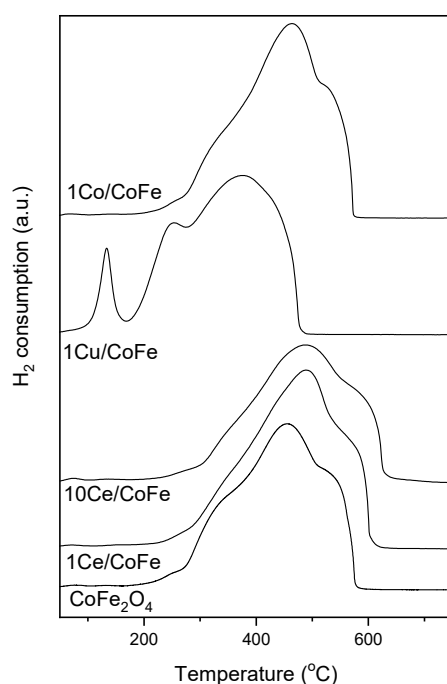

Figure 3. TPR (temperature programmed reduction) profiles for the indicated catalysts.

The top surface layers of the catalysts were examined by XPS. The spectra of Co 2p, Fe 2p, Ce 3d, Cu 2p$_{3/2}$, Zr 3d, and O 1s binding energy regions for the different samples are shown in Figure 4. Important constraints have been imposed for the fitting of these spectra and in order to get reliable quantitative estimations from them [26,27], as discussed in Supporting Information. They can be adequately fitted in the Co 2p$_{3/2}$ region with three peaks at ca. 780.0, 782.1, and 786.1 eV, and with relatively small differences between the samples, as will be discussed below. The two former peaks are attributed to Co^{2+} cations in octahedral and tetrahedral sites of the spinel structure, respectively [28]. In turn, the peak at ca. 786.1 eV corresponds to a satellite peak associated with the high spin Co^{2+} in the octahedral position [28]. The Fe 2p region XPS spectra exhibit peaks at ca. 710.9 and 724.5 eV, which correspond to Fe 2p$_{3/2}$ and Fe 2p$_{1/2}$ components. Considering exclusively the Fe 2p$_{3/2}$ region, the spectra are basically constituted by two peaks at ca. 710.7 and 713.2 eV, along with a satellite component that is broad and complex and displaying a maximum at ca. 718.0 eV. The former peaks are attributed to Fe^{3+} cations in the octahedral and tetrahedral sites of the spinel structure, respectively [28]. The satellite peak can in turn be basically related with the octahedral Fe^{3+} cations, considering that the (weak) maximum observed for such peak exhibits a shift higher than 7.0 eV with respect to corresponding photoelectron peak, more characteristic for that valence state than for Fe^{2+} species [29,30]. We cannot however discard, given the important width of the satellite contribution and its extension to lower binding energy, the presence of a residual part of the iron as Fe^{2+} species [28–30]. The spectra in the O 1s region are basically constituted by two peaks at ca. 529.9 and 530.7 eV (Figure 4). The first peak is assigned to lattice O^{2-} of the spinel structure [28]. The peak at 530.7 eV is broader and can be due to surface oxygen species or oxygen species in the proximity of lattice defects [28]. The Ce 3d spectra for 1Ce/CoFe and 10Ce/CoFe samples are displayed in Figure 4. Important differences are found between the two samples. Thus, the spectrum of 1Ce/CoFe can be mostly fitted with a set of two doublets in the 912–893 eV and 893–876 ranges, corresponding to 3d$_{3/2}$ and 3d$_{5/2}$ regions, respectively, and the spectrum is characteristic of Ce^{3+} [31,32]. Only a very small peak at ca. 917.0 eV, characteristic of Ce^{4+} (so called u''' component) [31,32], is detected, thus revealing that a small amount of Ce^{4+} is present too. In contrast, Ce^{4+} predominates in the Ce 3d spectrum of 10Ce/CoFe (with three sets of doublets for the two spin-orbit components), although introduction of two new peaks (emulating the peaks of Ce^{3+}) significantly enhances the fitting when imposing all Gaussian shapes. Indeed, the spectrum exhibits differences with that expected for pure CeO$_2$, strongly suggesting the presence of Ce^{3+} [31,32]. Thus, according to the fitting, about 31% of the cerium is as Ce^{3+}, which appears at a high reduction level in comparison with that observed for pure ceria nanoparticles [33]. On the other hand, the Cu 2p$_{3/2}$ region of 1Cu/CoFe displays a peak at ca. 933.1 eV along with a relatively small satellite component at ca. 943.9 eV (Figure 4). The weak intensity of such a satellite feature indicates the presence of a relatively small amount of Cu^{2+} in the sample [34,35]. In turn, the peak at 933.1 eV can mainly correspond to either Cu$^+$ or metallic copper species [34]. Analysis of the Cu$_{LMM}$ Auger zone (not shown) reveals a maximum at a kinetic energy of 914.9 eV, which corresponds to dispersed Cu$^+$ species [36–38], thus evidencing that this is the main state of most of the copper in the catalyst. Concerning the Zr 3d region in 1Zr/CoFe, it displays the two peaks characteristic for ZrO$_2$ at 182.2 eV (5/2 component) and 184.6 eV (3/2 component) [39].
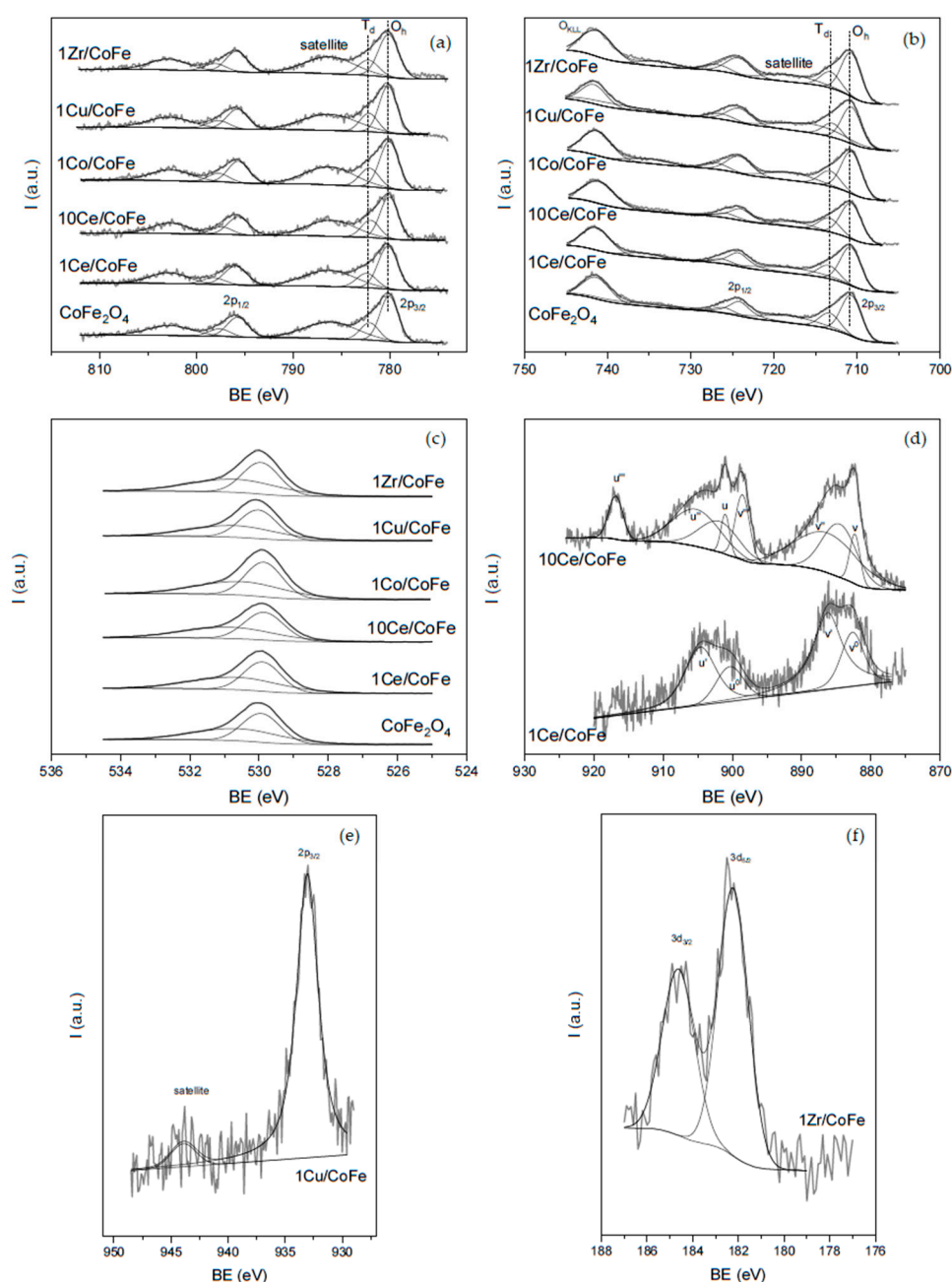
Figure 4. XPS (X-ray photoelectron spectra) for the indicated samples at regions (**a**) Co 2p; (**b**) Fe 2p; (**c**) O 1s; (**d**) Ce 3d; (**e**) Cu 2p$_{3/2}$; and (**f**) Zr 3d.

Table 2 collects data extracted from quantitative analysis of the intensity of observed XPS peaks, as determined from corresponding fitting of the spectra shown in Figure 4 (see also Supporting Information in Supplementary Materials). Atomic ratios for cobalt and iron reveal a ratio between them fairly close to the 1:2 stoichiometry of CoFe$_2$O$_4$ (an enrichment in iron is observed; note in any case that this can be strongly affected by even small differences in selected background lines during the fittings while errors in atomic sensitivity factors should be also considered). Among the samples, only a slightly higher amount of cobalt is observed in relative terms for 1Co/CoFe, which is expected taking into account the incorporation of extra cobalt at its surface. On the other hand, a decrease in both cobalt and iron detected for 10Ce/CoFe must be related to the attenuation of photoelectrons originated from the CoFe$_2$O$_4$ support in the presence of supported CeO$_2$ particles; indeed, a decrease in the overall intensity of photoelectrons from cobalt and

iron (2p regions in any case) of about 75% with respect to the bare $CoFe_2O_4$ support is observed for 10Ce/CoFe in the examined regions. In turn, the atomic ratios estimated for cerium or copper in 1 wt.% samples suggest they achieve a relatively high dispersion degree over the $CoFe_2O_4$ support, higher for cerium in 1Ce/CoFe, taking into account its lower atomic loading. In contrast, a low dispersion level is inferred for zirconium from analysis of corresponding atomic ratio and in agreement with TEM results exposed above. Comparison of the relative amount of cerium detected between 1Ce/CoFe and 10Ce/CoFe reveals the lower overall dispersion of cerium in the latter, consistent with the formation of ceria particles in a significant amount in it, in accordance with the structural results described above (Figures 1 and 2).

Table 2. Ratios extracted from quantitative analysis of the XPS fitted spectra. Atomic sensitivity factors employed to determine atomic ratios were taken from Wagner et al. [40].

Catalyst	[Co]/([Co] + [Fe] + [O])	[Fe]/([Co] + [Fe] + [O])	[M [a]]/([Co] + [Fe] + [O])	O/T [b] (Co 2p)	O/T [b] (Fe 2p)	sat./main [c]
$CoFe_2O_4$	0.104	0.268	-	0.72/0.28	0.72/0.28	0.765
1Ce/CoFe	0.102	0.246	0.0189	0.75/0.25	0.74/0.26	0.723
10Ce/CoFe	0.0873	0.218	0.0599	0.71/0.29	0.72/0.28	0.714
1Co/CoFe	0.113	0.246	-	0.72/0.28	0.73/0.27	0.709
1Cu/CoFe	0.104	0.236	0.0189	0.72/0.28	0.72/0.28	0.711
1Zr/CoFe	0.103	0.240	0.00679	0.74/0.26	0.73/0.27	0.708

[a] M = Ce, Cu, or Zr. [b] Ratio between the intensities of peaks attributed to octahedral and tetrahedral species (see main text). [c] Ratio between the intensities of satellite and main photoelectron peaks in Co 2p region.

On the other hand, the ratio between octahedral and tetrahedral cobalt (or iron) species confirms that the $CoFe_2O_4$ spinel structure presents a partial inversion degree, as typically observed for this spinel [11,12,26–28]; note even for strongly sintered specimens, the thermodynamically favored fully inverse configuration is difficult to be achieved in any case [11,28,41]. Considering the cobalt species, about 70% appears in the octahedral position. This would theoretically correspond to about 65% of the iron in the octahedral position. However, the amount of iron estimated from XPS in such a position appears a little higher than 65%. The origin of this discrepancy can be the presence of a small amount of Co^{3+} overlapping with the octahedral Co^{2+} contribution. Note in this sense that it is typically not easy to distinguish the cobalt valence state on the basis of only the BE position of the main line [42,43]. Another approach in this sense is analyzing the relative contribution of the satellite feature, since Co^{3+} compounds show practically no satellite line, while it is typically more shifted with respect to the main photoelectron line than that of Co^{2+} [29,42,43]. Direct comparison with results in the literature is not possible in this sense since the fitting procedure employed in each case is not uniform. However, within the series examined with our method, it is noted that the relative contribution of the Co 2p satellite line decreases slightly (and its maximum, even if very slightly, shifts to higher BE) for samples in which metals have been introduced at the surface of $CoFe_2O_4$. Such a decrease cannot be correlated with the relative amount of octahedral high spin Co^{2+} species present in each case. Alternatively, it strongly suggests the presence of a higher amount of surface Co^{3+} species in such modified samples. This can be a consequence of the impregnation step employed to incorporate the metal on the $CoFe_2O_4$ surface. Since the point of zero charge of $CoFe_2O_4$ is pH_{PZC} = 8.0 [44], the acid impregnating solution of the metal salt can, even if to a limited extent, dissolve the surface cations of $CoFe_2O_4$. They then become readsorbed and integrate to the final solid during the impregnation/drying/calcination steps. Then, the cobalt cations leached from the support can finally form Co^{3+} species dispersed (along with the heterocations or extra cobalt added) on the surface of $CoFe_2O_4$. It must be also considered that the theoretical coverage of the metals added by impregnation in 1 wt.% samples is relatively low. For instance, in the case of 1Ce/CoFe, taking into account the $CoFe_2O_4$ S_{BET} (Table 1) and about 3 Ce^{3+} cations every 0.065 nm^2 in Ce_2O_3 [45], it would

be about 15% of a monolayer; in the most extreme case that atomically dispersed cerium would be achieved, it must be considered that the amount of cerium cations incorporated to the catalyst would be about 40% of the theoretical amount of surface exposed cobalt cations (if they were at all exposed), considering a lattice parameter for the $CoFe_2O_4$ unit cell of ca. 8.35 Å. In turn, in the case of cobalt or copper in 1 wt.% samples, the theoretical coverage would lie between about 25% of a monolayer in condensed oxide phases and 90% in most dispersed (atomically) state. Then, less than a monolayer coverage is expected in any case for the 1 wt.% samples. In addition, it must be taken into account that a region of a few nanometers with several atomic layers can be sampled within Co 2p or Fe 2p photoelectrons collected when using Mg Kα excitation. Thus, only a minor fraction of the sampled cobalt or iron is expected to be affected by direct interaction with the deposited metals while mentioned leaching/readsorption of cobalt or iron cations during impregnation must be limited in any case, given that only minor changes are observed between the samples in corresponding regions. In the case of zirconium for 1Zr/CoFe, its atomic ratio reveals a very low dispersion degree of zirconium in this sample, in agreement with its presence basically forming big zirconia crystals, as discussed above.

In definitive, characterization results show that $CoFe_2O_4$ presents the spinel structure and forms aggregates of crystals with 18 nm average size, which constitute a mesoporous structure. XPS results are consistent with partial inversion of the spinel structure, in agreement with results in the literature [11,12,26–28]. Incorporation of metals like cerium, cobalt, copper, and zirconium on the $CoFe_2O_4$ surface by impregnation apparently induces some changes at the surface of $CoFe_2O_4$, on the basis of mainly XPS analysis. In particular, a process of leaching/readsorption of surface cations of the support may occur during the preparation steps of the supported metal catalysts, which can finally result in the formation of dispersed Co^{3+} species over the $CoFe_2O_4$ support. This is also consistent with the shift observed in the reduction of the support according to the TPR results. Thus, in the case of 1Cu/CoFe, an important shift to lower temperatures in the reduction of $CoFe_2O_4$ has been observed as a consequence of hydrogen activation on metallic copper formed at relatively low reduction temperatures. However, the reduction of dispersed Co^{3+} species is expected to be produced above 300 °C at temperatures overlapping those of $CoFe_2O_4$ reduction [25]. The presence of dispersed Co^{3+} on the surface of $CoFe_2O_4$ can then hinder hydrogen activation and lead to a shift of the $CoFe_2O_4$ reduction to higher temperatures. Note also in this sense the higher width of $CoFe_2O_4$ reduction peaks in the supported metal samples, which could be related to the overlap with dispersed Co^{3+} reduction taking place simultaneously (Figure 3). In turn, within the redox interplay taking place between the different redox cations during the impregnation/drying/calcination steps employed for preparation of the supported specimens, the results reveal that the dispersed incorporated heterometal in the final calcined material appears mostly as reduced or partially reduced entity. Thus, copper in 1Cu/CoFe appears mostly as dispersed Cu^+ entities with only a small part as Cu^{2+}. The same occurs for cerium in 1Ce/CoFe, which basically appears as dispersed Ce^{3+} entities. Furthermore, even for the 10Ce/CoFe sample, about 31% of the cerium appears as Ce^{3+}, which appears higher than expected for pure ceria nanoparticles, thus suggesting in any case a reduction effect of the $CoFe_2O_4$ support on the supported entities.

2.2. Catalytic Properties

The catalytic performance of the various catalysts for the CO-PROX process (CO conversion and O_2 selectivity to CO_2) as a function of temperature is displayed in Figure 5. CO conversion over $CoFe_2O_4$ exhibits an irregular shape with a first low temperature CO oxidation process, which appears affected by deactivation. Thus, while CO conversion starts at ca. 48% at the lowest examined temperature (35 °C), it decreases down to ca. 30% at 150 °C. It then increases to ca. 50% conversion with increasing temperature up to 250 °C, and finally decreases above this temperature. It must be noted that maximum CO conversion achieved over this system (around 50%), is much lower than 100% conversion required

for practical application. This contrasts with full conversion achieved, for instance, over catalysts combining copper and ceria tested under the same conditions in our group [21,38]. It must be noted in this sense that higher conversion level, even full CO conversion, can be achieved also over $CoFe_2O_4$-related systems, although it requires employment of lower spatial velocity than used here [17,18]. The relatively low CO conversion level achieved over $CoFe_2O_4$ under the examined conditions prompted us to attempt to enhance the activity of the system upon including possible promoters on its surface as in the $M/CoFe_2O_4$ catalysts here explored. Indeed, except for the low temperature maximum observed over $CoFe_2O_4$ at 35 °C (a process which appears much more limited over the $M/CoFe_2O_4$ systems), all the examined $M/CoFe_2O_4$ enhance the CO conversion performance of the bare $CoFe_2O_4$ system to different extents and with the only exception of 1Cu/CoFe, for which the promoting effect appears limited by an intermediate deactivation step in the range of 225–275 °C. Thus, the presence of cerium on $CoFe_2O_4$ apparently enhances its CO oxidation performance, and the activity apparently increases with the cerium content. In turn, an important enhancement of the CO oxidation activity of $CoFe_2O_4$ is observed upon incorporation of a small amount of cobalt on its surface in the 1Co/CoFe catalyst or of zirconium in 1Zr/CoFe. On the other hand, the 1Cu/CoFe sample constitutes a particular case, since it is the only sample exhibiting some methanation activity (according to observation of methane in the detection by infrared–intense bands centered at ca. 1305 and 3020 cm^{-1}–and MS signal at m/e = 15) at 250 °C and above. This process motivates the final increase in CO conversion observed at these temperatures over this catalyst.

Concerning the selectivity of O_2 to CO_2, all catalysts show full selectivity at low temperature and a final decrease at high temperature, which is basically related to competition between CO and H_2 for their oxidation with available oxygen, as typically observed for CO-PROX catalysts [17,21,38]. $CoFe_2O_4$ is the system which exhibits highest selectivity, while $M/CoFe_2O_4$ show somewhat lower selectivity at high temperatures, with 1Cu/CoFe showing the lowest selectivity values among the catalysts.

Further examination of selected systems was made by means of operando-DRIFTS and in order to get more hints about the catalytic behavior observed for them. Corresponding results are shown in Figure 6. The main observed bands and changes upon interaction with the CO-PROX mixture occur in the spectral zone of stretching vibrations of complexes with O-C-O fragments (basically carbonate-type species) which is the region displayed in Figure 6. A set of common bands is identified in the examined catalysts. Thus, bands at ca. 1615, 1417, and 1219 cm^{-1}, attributable to bicarbonate species [17], appear in all cases upon interaction of the CO-PROX reaction mixture with the samples at 25 °C, and decrease and finally vanish upon increasing the reaction temperature. In turn, broad bands centered at ca. 1494 and 1348 cm^{-1} (shifted to the blue for 10Ce/CoFe, most likely due to the fact that they are mostly formed over the ceria component in this sample [46,47]), which can be due to polydentate carbonate species [17,46], are also observed at low reaction temperatures and do not change strongly (or even somewhat increase) upon increasing the temperature under the CO-PROX mixture. Some additional bands at 1567, 1532, and 1253 cm^{-1} are apparent in the case of 1Zr/CoFe and 1Co/CoFe, which can be due to any type of carbonate species; note that in no case formate species, which would give rise to characteristic bands related to C-H vibration in the 3000–2800 cm^{-1} region, are observed under examined conditions. In turn, bands attributable to bidentate carbonates at ca. 1580 and 1300 cm^{-1} are observed at low reaction temperatures over 10Ce/CoFe [46,47]. All these carbonate-type features may well reflect the interaction of CO_2 generated during the reaction with the sample surface in each case.
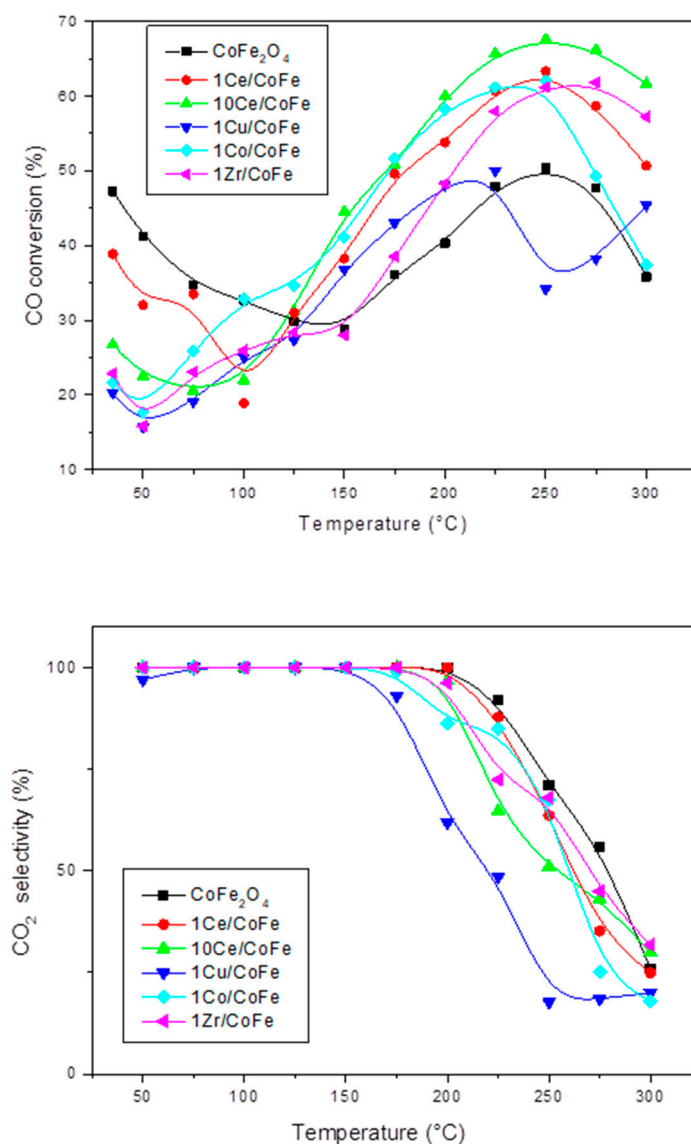
Figure 5. Catalytic activity results observed for the indicated catalysts under CO preferential oxidation (CO-PROX) conditions (1% CO, 1.25% O_2, 50% H_2 and 0.2% H_2O in He at 80,000 h^{-1}). Top: CO conversion; Bottom: O_2 selectivity to CO_2.

The formation of metal carbonyls apparently occurs only in the case of 1Cu/CoFe, Figure 7. Thus, a band at ca. 2112 cm^{-1}, which in agreement with XPS analysis above is attributable to Cu^+ carbonyls [21,38,48], appears already upon first contact with the reactant mixture at 25 °C. This band grows up to 100 °C, at which point a carbonyl at 2103 cm^{-1} appears. This latter may well be related to another Cu^+-carbonyl species given its relatively high thermal stability [46]. Both carbonyls importantly decrease above 100 °C, the latter displaying an apparently higher stability.
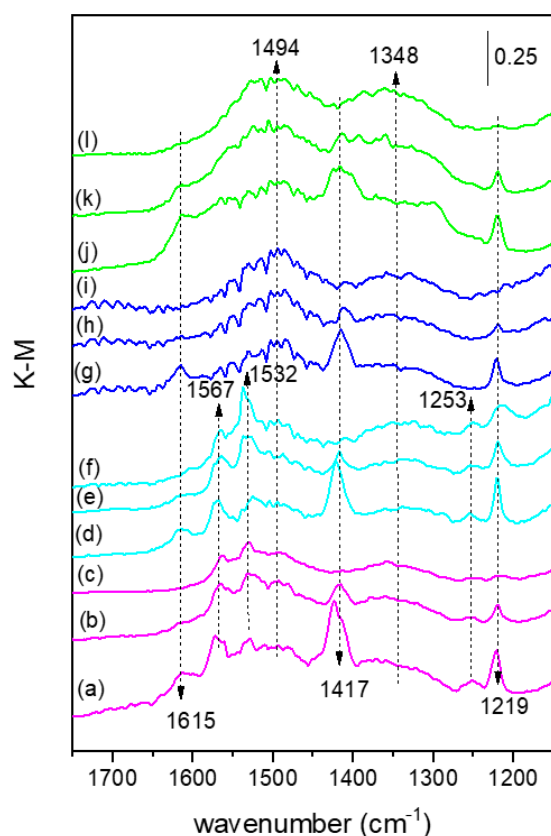
Figure 6. DRIFTS spectra under CO-PROX conditions for the following samples and reaction temperatures. (**a**) 1Zr/CoFe, 25 °C; (**b**) 1Zr/CoFe, 125 °C; (**c**) 1Zr/CoFe, 250 °C; (**d**) 1Co/CoFe, 25 °C; (**e**) 1Co/CoFe, 125 °C; (**f**) 1Co/CoFe, 250 °C; (**g**) 1Cu/CoFe, 25 °C; (**h**) 1Cu/CoFe, 125 °C; (**i**) 1Cu/CoFe, 250 °C; (**j**) 10Ce/CoFe, 25 °C; (**k**) 10Ce/CoFe, 125 °C; (**l**) 10Ce/CoFe, 250 °C.
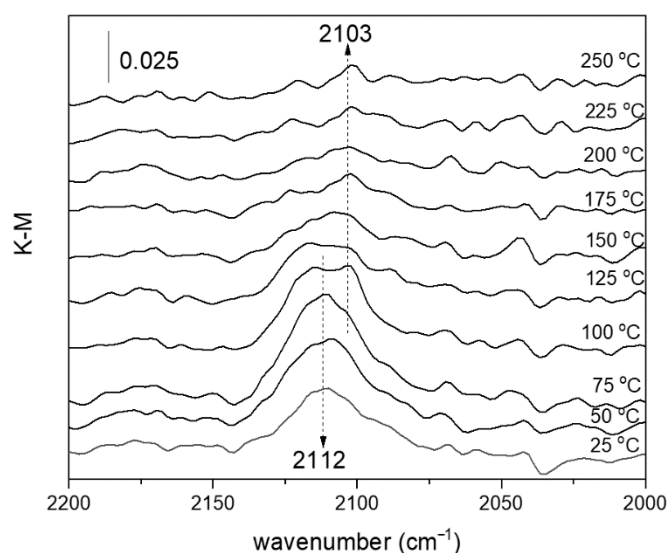

Figure 7. DRIFTS spectra under CO-PROX conditions for 1Cu/CoFe at indicated temperatures.

Important modifications of the CO-PROX performance are observed in the presence of the various metals on the surface of $CoFe_2O_4$. First, the CO oxidation activity observed at low temperature (below ca. 100 °C) over $CoFe_2O_4$ is apparently decreased (Figure 5). Only 1Ce/CoFe keeps a certain activity in that range while the rest exhibit an important

decrease. The low temperature CO oxidation activity of $CoFe_2O_4$, in a deactivated process most likely caused by the presence of residual water in the reactant mixture [22], can be due to the presence of octahedral Co^{2+} species, in accordance with XPS results (Figure 4), which become oxidized under reaction conditions to form the active Co^{3+} species [9]. The decrease observed in this activity upon incorporation of the metals must be related to the modifications induced in the octahedral Co^{2+} species of $CoFe_2O_4$. As discussed above, this can be related to the interaction of the $CoFe_2O_4$ surface with the acid impregnating solution in each case. The fact that 1Ce/CoFe is the least affected supports this hypothesis taking into account that the impregnating solution employed in this case is expected to be less acidic than for the other modified systems, and therefore the one expected to produce a lower modification of the $CoFe_2O_4$ surface. This correlates as well with the fact that 1Ce/CoFe shows the highest satellite to main ratio in Co 2p XPS (Table 2), and therefore the lowest presence of surface Co^{3+} species among the modified catalysts, according to the discussion above. These modifications, and in particular the formation of Co^{3+} species in the $M/CoFe_2O_4$ samples, can in turn explain the enhancement observed in CO conversion above ca. 150 °C for all modified samples, while the establishment of interactions between cobalt and cerium can also contribute to such enhancement in corresponding catalysts [22]. Nevertheless, the case of 1Cu/CoFe constitutes a particular one. First, it shows relatively lower CO_2 selectivity. This can be due to the facility for copper reduction to metallic copper, in agreement with TPR exploration (Figure 3), known to be less selective than oxidized states of copper [47]. This is supported by the DRIFTS experiments (Figure 7) since the important decrease of Cu^+ carbonyls above ca. 100 °C basically reflects the formation of metallic copper over which carbonyls are less stable and difficult to be observed under examined conditions [38,47,48]. On the other hand, 1Cu/CoFe is the only catalyst which displays some methanation activity, above 250 °C. Copper catalysts, in contrast to cobalt ones, do not typically show methanation activity under CO-PROX conditions [17,38,47,49]. Thus, such activity must be related to achievement, upon promotion by copper, of reduced states of cobalt active for such reaction [17], in agreement with the analysis of TPR results.

3. Materials and Methods

$CoFe_2O_4$ was prepared by a sol-gel method by adding citric acid (from Merck, Darmstadt, Germany) in excess ($3 \times [Fe^{3+} + Co^{2+}]$) to an aqueous solution of cobalt and iron nitrates with the appropriate molar ratios. The mixture was kept under stirring at 80 °C until complete evaporation of the liquid. The resulting gel was dried over night at 100 °C and finally calcined at 500 °C for 4 h. Five catalysts of Cu, Ce, Co, and Zr supported on $CoFe_2O_4$ were prepared by incipient wetness impregnation of the $CoFe_2O_4$ support using aqueous solutions of cerium (III) nitrate hexahydrate to give final cerium loading of 1 and 10 wt% and copper (II), cobalt (III), and zirconyl nitrates to give a final loading of 1 wt.% in any case (all reagents from Sigma-Aldrich, St. Louis, MO, USA). We chose such relatively low loading with the aim of promoting the reactivity of $CoFe_2O_4$ rather than introducing new active entities inducing new functionalities to the system. In the case of the cerium promoter, previous work shows that new functionalities of the support or support-ceria interface are provided upon increasing the cerium loading, and this prompted us to prepare a second catalyst with higher loading [21]. Following impregnation, the samples were dried overnight at 120 °C and calcined under air at 500 °C (5 °C min^{-1} ramp) for 2 h. These samples will be referred to as M/CoFe with M = 1%Co, 1%Zr, 1%Cu, 1%Ce, and 10%Ce.

The specific surface area of the calcined catalysts was determined by the BET method. N_2 adsorption isotherms were recorded with a Micromeritics 2100 automatic apparatus at liquid nitrogen temperature. The catalysts were degassed at 180 °C for 12 h before measurement of corresponding isotherms.

The X-ray photoelectron spectra (XPS) of the catalysts were collected using a Specs Gmbh spectrometer under ultra-high vacuum conditions and using Mg Kα radiation and a Phoibos1509MCD energy analyzer. Binding energy values were estimated by using as reference the C 1s peak of contaminant carbon at 285.0 eV; in samples containing cerium,

such correction was further checked by adjusting the characteristic u''' peak of Ce 3d to 917.0 eV [50]. The XPSPeak 4.1 software was used for the analysis of spectra.

High resolution transmission electron microscopy (HRTEM) data and X-ray energy dispersive spectra (XEDS) were recorded on a JEOL TEM/STEM 2100F field emission gun transmission electron microscope operating at 200 kV and equipped with an EDS spectrometer Oxford INCA X-sight system. XEDS analysis was performed in STEM mode. Specimens were prepared by depositing small portions of the samples to be investigated from ethanol dispersion onto a nickel grid supporting a perforated carbon film.

Temperature programmed reduction (TPR) was measured in a flow system using 5% H_2/He premixed gas with a flow rate of 30 mL min^{-1}. About 250 mg of the catalyst was placed into a glass tube and pretreated under 10% O_2/He at 500 °C for 1 h using 100 mL min^{-1} flow rate and 10 °C min^{-1} ramp. The sample was then cooled to room temperature, thoroughly purged with inert gas and, after switching to the reducing gas mixture, it was heated up to 500 °C using 10 °C min^{-1} ramp. A Micromeritics Autochem II 2920 apparatus fitted with a TCD detector was employed for this measurement.

For the CO-PROX reaction, the catalysts calcined in situ (under oxygen diluted in He at 500 °C) were tested in a glass tubular catalytic reactor for their activity under an atmospheric pressure flow (using mass flow controllers to prepare the reactant mixture) of 1% CO, 1.25% O_2, and 50% H_2 with 0.2% H_2O (He balance) [21], at a rate of 1000 cm^3 min^{-1} g^{-1} (roughly corresponding to 80,000 h^{-1} GHSV) and using a heating ramp of 5 °C min^{-1}. These conditions are the same as employed previously for related catalysts of copper and which we keep in order to allow direct comparison [21]. Analysis of the feed and outlet gas streams was done by gas infrared (Bruker Equinox 55 FTIR spectrometer, coupled to a multiple reflection transmission cell-Infrared Analysis Inc. "long path gas mini cell", 2.4 m path length, ca. 130 cm^3 internal volume) and mass spectrometry (Pfeiffer Omnistar). In most of the catalysts (1Cu/CoFe the only exception), no products other than those resulting from CO or H_2 combustion (i.e., CO_2 and H_2O; note that possible contributions of WGS or reverse WGS must be residual under the conditions employed and, if at all, would take place only at temperatures higher than ca. 200 °C over this type of catalysts) were detected in the course of the runs, in agreement with previous results on catalysts of this type [21]. On this basis, in those cases values of percentage conversion and selectivity in the CO-PROX process are defined as:

$$X_{CO} = \frac{F_{CO}^{in} - F_{CO}^{out}}{F_{CO}^{in}} \times 100 \tag{1}$$

$$S_{CO_2} = \frac{X_{CO}}{2.5 X_{O_2}} \times 100 \tag{2}$$

$$X_{O_2} = \frac{F_{O_2}^{in} - F_{O_2}^{out}}{F_{O_2}^{out}} \times 100 \tag{3}$$

where X and S are percentage conversion and selectivity, respectively, and F is the (inlet or outlet) molar flow of the indicated gas.

DRIFTS experiments under reaction conditions were carried out using a Bruker Equinox 55 FTIR spectrometer fitted with an MCT detector. The DRIFTS cell (Harrick) was fitted with CaF_2 windows and a heating cartridge that allowed samples to be heated to 500 °C. Aliquots of ca. 100 mg were calcined in situ (in a similar way as employed for the catalytic tests) and then cooled to room temperature under diluted oxygen before introducing the reaction mixture and heating under a 5 °C min^{-1} ramp, recording typically one spectrum (accumulating 20 scans) every 20 °C. The gas mixture (1% CO + 1.25% O_2 + 50% H_2 with 0.2% H_2O in He, the same as that employed for the catalytic activity tests) was prepared using mass flow controllers with ca. 100 cm^3 min^{-1} passing through the catalyst bed at atmospheric pressure, which corresponds to conditions similar to those employed for the activity tests performed with the tubular reactor.

4. Conclusions

A $CoFe_2O_4$ catalyst has been prepared by sol-gel, characterized with a multi-technique approach, and employed for preferential oxidation of CO in a H_2-rich stream (CO-PROX). In turn, catalysts $M/CoFe_2O_4$, in which Ce, Co, Cu, and Zr are introduced at the surface of $CoFe_2O_4$ by impregnation, have been similarly examined. Characterization of the catalysts by N_2 adsorption, XRD, and HRTEM show that $CoFe_2O_4$ forms a mesoporous structure composed by crystals of about 18 nm with the partially inverse spinel structure, as confirmed by XPS, on which the various mentioned metals become dispersed to different degrees. It is noted, on the basis of detailed XPS analysis, that the impregnation process employed to introduce mentioned metals modifies the surface of $CoFe_2O_4$, increasing the amount of surface Co^{3+} species on them. This induces important modifications in the CO-PROX performance of the catalyst. On the one hand, a deactivated low temperature CO oxidation process observed over $CoFe_2O_4$ becomes hindered in $M/CoFe_2O_4$. On the other hand, the CO oxidation appears importantly promoted above 125 °C in $M/CoFe_2O_4$ systems. Among the examined catalysts, only the $Cu/CoFe_2O_4$ catalyst exhibits some methanation activity above 250 °C, which is attributed to the relatively strong degree of reduction achieved in the presence of copper which in turn favors cobalt reduction, in agreement with DRIFTS analysis under reaction conditions and TPR exploration.

References

1. Dinçer, I.; Zamfirescu, C. *Sustainable Energy Systems and Applications*; Springer: New York, NY, USA, 2012; pp. 519–632.
2. Sørensen, B. *Hydrogen and Fuel Cells: Emerging Technologies and Applications*; Academic Press: Cambridge, MA, USA, 2012.
3. Debe, M.K. Electrocatalyst approaches and challenges for automotive fuel cells. *Nature* **2012**, *486*, 43–51. [CrossRef] [PubMed]
4. Kalamaras, C.M.; Efstathiou, A.M. Hydrogen Production Technologies: Current State and Future Developments. In *Conference Papers in Energy*; Hindawi Publishing Corporation: London, UK, 2013; Volume 2013, p. 690627.
5. Nikolaidis, P.; Poullikkas, A. A comparative overview of hydrogen production processes. *Renew. Sustain. Energy Rev.* **2017**, *67*, 597–611. [CrossRef]
6. Konsolakis, M.; Lykaki, M. Recent Advances on the Rational Design of Non-Precious Metal Oxide Catalysts Exemplified by CuO_x/CeO_2 Binary System: Implications of Size, Shape and Electronic Effects on Intrinsic Reactivity and Metal-Support Interactions. *Catalysts* **2020**, *10*, 160. [CrossRef]
7. Jing, P.; Gong, X.; Liu, B.; Zhang, J. Recent advances in synergistic effect promoted catalysts for preferential oxidation of carbon monoxide. *Catal. Sci. Technol.* **2020**, *10*, 919–934. [CrossRef]
8. Bion, N.; Epron, F.; Moreno, M.; Mariño, F.; Duprez, D. Preferential Oxidation of Carbon Monoxide in the Presence of Hydrogen (PROX) over Noble Metals and Transition Metal Oxides: Advantages and Drawbacks. *Top. Catal.* **2008**, *51*, 76–88. [CrossRef]
9. Gu, D.; Jia, C.-J.; Weidenthaler, C.; Bongard, H.-J.; Spliethoff, B.; Schmidt, W.; Schüth, F. Highly Ordered Mesoporous Cobalt-Containing Oxides: Structure, Catalytic Properties, and Active Sites in Oxidation of Carbon Monoxide. *J. Am. Chem. Soc.* **2015**, *137*, 11407–11418. [CrossRef]
10. Baidya, T.; Murayama, T.; Nellaiappan, S.; Katiyar, N.K.; Bera, P.; Safonova, O.; Lin, M.; Priolkar, K.R.; Kundu, S.; Rao, B.S.; et al. Ultra-Low-Temperature CO Oxidation Activity of Octahedral Site Cobalt Species in Co_3O_4 Based Catalysts: Unravelling the Origin of the Unique Catalytic Property. *J. Phys. Chem. C* **2019**, *123*, 19557–19571. [CrossRef]

11. Sawatzky, G.A.; van der Woude, F.; Morrish, A.H. Cation Distributions in Octahedral and Tetrahedral Sites of the Ferrimagnetic Spinel CoFe$_2$O$_4$. *J. Appl. Phys.* **1968**, *39*, 1204–1206. [CrossRef]

12. Carta, D.; Casula, M.F.; Falqui, A.; Loche, D.; Mountjoy, G.; Sangregorio, C.; Corrias, A. A Structural and Magnetic Investigation of the Inversion Degree in Ferrite Nanocrystals MFe$_2$O$_4$ (M = Mn, Co, Ni). *J. Phys. Chem. C* **2009**, *113*, 8606–8615. [CrossRef]

13. Cao, J.-L.; Yan, Z.-L.; Wang, Y.; Sun, G.; Wang, X.; Bala, H.; Zhang, Z.-Y. CTAB-assisted synthesis of mesoporous CoFe$_2$O$_4$ with high carbon monoxide oxidation activity. *Mater. Lett.* **2013**, *106*, 322–325. [CrossRef]

14. Kouotou, P.M.; Vieker, H.; Tian, Z.Y.; Ngamou, P.H.T.; el Kasmi, A.; Beyer, A.; Gölzhäuser, A.; Kohse-Höinghaus, K. Structure–activity relation of spinel-type Co–Fe oxides for low-temperature CO oxidation. *Catal. Sci. Technol.* **2014**, *4*, 3359–3367. [CrossRef]

15. Thomas, J.; Thomas, N.; Girgsdies, F.; Beherns, M.; Huang, X.; Sudheesh, V.D.; Sebastian, V. Synthesis of cobalt ferrite nanoparticles by constant pH co-precipitation and their high catalytic activity in CO oxidation. *New J. Chem.* **2017**, *41*, 7356–7663. [CrossRef]

16. Biabani-Ravandi, A.; Rezaei, M. Low temperature CO oxidation over Fe–Co mixed oxide nanocatalysts. *Chem. Eng. J.* **2012**, *184*, 141–146. [CrossRef]

17. Chagas, C.A.; de Souza, E.F.; de Carvalho, M.C.N.A.; Martins, R.L.; Schmal, M. Cobalt ferrite nanoparticles for the preferential oxidation of CO. *Appl. Catal. A* **2016**, *519*, 139–145. [CrossRef]

18. Qwabe, L.Q.; Friedrich, H.B.; Singh, S. Preferential oxidation of CO in a hydrogen rich feed stream using Co–Fe mixed metal oxide catalysts prepared from hydrotalcite precursors. *J. Mol. Catal. A* **2015**, *404–405*, 167–177. [CrossRef]

19. Venturini, J.; Wermuth, T.B.; Machado, M.C.; Arcaro, S.; Alves, A.K.; Viegas, A.d.; Bergmann, C.P. The influence of solvent composition in the sol-gel synthesis of cobalt ferrite (CoFe$_2$O$_4$): A route to tuning its magnetic and mechanical properties. *J. Eur. Ceram. Soc.* **2019**, *39*, 3442–3449. [CrossRef]

20. Chen, X.; Wu, C.; Guo, Z. Synthesis of Efficient Cu/CoFe$_2$O$_4$ Catalysts for Low Temperature CO Oxidation. *Catal. Lett.* **2019**, *149*, 399–409. [CrossRef]

21. Elmhamdi, A.; Pascual, L.; Nahdi, K.; Martínez-Arias, A. Structure/redox/activity relationships in CeO$_2$/CuMn$_2$O$_4$ CO-PROX catalysts. *Appl. Catal. B* **2017**, *217*, 1–11. [CrossRef]

22. Bolívar-Díaz, C.L.; Conesa, J.C.; Corberán, V.C.; Monte, M.; Martínez-Arias, A. Nanostructured Catalysts Based on Combinations of Cobalt and Cerium Oxides for CO Oxidation and Effect of the Presence of Water. *J. Nanosci. Nanotechnol.* **2017**, *17*, 3816–3823. [CrossRef]

23. Brown, R.; Cooper, M.E.; Whan, D.A. Temperature programmed reduction of alumina-supported iron, cobalt and nickel bimetallic catalysts. *Appl. Catal.* **1982**, *3*, 177–186. [CrossRef]

24. Hammiche-Bellal, Y.; Djadoun, A.; Meddour-Boukhobza, L.; Benadda, A.; Auroux, A.; Berger, M.-H.; Mernache, F. Effect of the preparation method on the structural and catalytic properties of spinel cobalt-iron oxide. *Mater. Chem. Phys.* **2016**, *177*, 384–397. [CrossRef]

25. Wang, W.-J.; Lin, H.-Y.; Chen, Y.-W. Carbon Monoxide Hydrogenation on Cobalt/Zeolite Catalysts. *J. Porous Mater.* **2005**, *12*, 5–12. [CrossRef]

26. Fantauzzi, M.; Secci, F.; Angotzi, M.S.; Passiu, C.; Cannas, C.; Rossi, A. Nanostructured spinel cobalt ferrites: Fe and Co chemical state, cation distribution and size effects by X-ray photoelectron spectroscopy. *RSC Adv.* **2019**, *9*, 19171–19179. [CrossRef]

27. Aghavnian, T.; Moussy, J.-B.; Stanescu, D.; Belkhou, R.; Jedrecy, N.; Magnan, H.; Ohresser, P.; Arrio, M.-A.; Sainctavit, P.; Barbier, A. Determination of the cation site distribution of the spinel in mulltiferroic CoFe$_2$O$_4$/BaTiO$_3$ layers by X-ray photoelectron spectroscopy. *J. Electron Spectrosc. Relat. Phenom.* **2015**, *202*, 16–21. [CrossRef]

28. Zhou, Z.; Zhang, Y.; Wang, Z.; Wei, W.; Tang, W.; Shi, J.; Xiong, R. Electronic structure studies of the spinel CoFe$_2$O$_4$ by X-ray photoelectron spectroscopy. *Appl. Surf. Sci.* **2008**, *254*, 6972–6975. [CrossRef]

29. Allen, G.C.; Harris, S.J.; Jutson, J.A.; Dyke, J.M. A study of a number of mixed transition metal oxide spinels using X-ray photoelectron spectroscopy. *Appl. Surf. Sci.* **1989**, *37*, 111–134. [CrossRef]

30. Grosvenor, A.P.; Kobe, B.A.; Biesinger, M.C.; McIntyre, N.S. Investigation of multiplet splitting of Fe 2p XPS spectra and bonding in iron compounds. *Surf. Interface Anal.* **2004**, *36*, 1564–1574. [CrossRef]

31. Holgado, J.P.; Alvarez, R.; Munuera, G. Study of CeO$_x$ XPS spectra by factor analysis: Reduction of CeO$_2$. *Appl. Surf. Sci.* **2000**, *161*, 301–315. [CrossRef]

32. Paparazzo, E. Use and mis-use of x-ray photoemission spectroscopy Ce3d spectra of Ce$_2$O$_3$ and CeO$_2$. *J. Phys. Condens. Matter* **2018**, *30*, 343003. [CrossRef]

33. Zhou, X.-D.; Huebner, W. Size-induced lattice relaxation in CeO$_2$ nanoparticles. *Appl. Phys. Lett.* **2001**, *79*, 3512–3514. [CrossRef]

34. Svintsitskiy, D.A.; Kardash, T.Y.; Stonkus, O.A.; Slavinskaya, E.M.; Stadnichenko, A.I.; Koscheev, S.V.; Chupakhin, A.P.; Boronin, A.I. In Situ XRD, XPS, TEM, and TPR Study of Highly Active in CO Oxidation CuO Nanopowders. *J. Phys. Chem. C* **2013**, *117*, 14588–14599. [CrossRef]

35. Monte, M.; Munuera, G.; Costa, D.; Conesa, J.C.; Martínez-Arias, A. Near-ambient XPS characterization of interfacial copper species in ceria-supported copper catalysts. *Phys. Chem. Chem. Phys.* **2015**, *17*, 29995–30004. [CrossRef] [PubMed]

36. Grünert, W.; Hayes, N.W.; Joyner, R.W.; Shpiro, E.S.; Rafiq, M.; Siddiqui, H.; Baeva, G.N. Structure, Chemistry, and Activity of Cu-ZSM-5 Catalysts for the Selective Reduction of NOx in the Presence of Oxygen. *J. Phys. Chem.* **1994**, *98*, 10832–10846. [CrossRef]

37. Morales, J.; Espinos, J.P.; Caballero, A.; Gonzalez-Elipe, A.R.; Mejias, J.A. XPS Study of Interface and Ligand Effects in Supported Cu$_2$O and CuO Nanometric Particles. *J. Phys. Chem. B* **2005**, *109*, 7758–7765. [CrossRef] [PubMed]

38. Gamarra, D.; Cámara, A.L.; Monte, M.; Rasmussen, S.B.; Chinchilla, L.E.; Hungría, A.B.; Munuera, G.; Gyorffy, N.; Schay, Z.; Corberán, V.C.; et al. Preferential oxidation of CO in excess H_2 over CuO/CeO_2 catalysts: Characterization and performance as a function of the exposed face present in the CeO_2 support. *Appl. Catal. B* **2013**, *130–131*, 224–238. [CrossRef]

39. Morant, C.; Sanz, J.M.; Galán, L.; Soriano, L.; Rueda, F. An XPS Study of the Interaction of Oxygen with Zirconium. *Surf. Sci.* **1989**, *218*, 331–345. [CrossRef]

40. Wagner, C.D.; Davis, L.E.; Zeller, M.V.; Taylor, J.A.; Raymond, R.H.; Gale, L.H. Empirical Atomic Sensitivity Factors for Quantitative Analysis by Electron Spectroscopy for Chemical Analysis. *Surf. Interf. Anal.* **1981**, *3*, 211–225. [CrossRef]

41. Hou, Y.H.; Zhao, Y.J.; Liu, Z.W.; Yu, H.Y.; Zhong, X.C.; Qiu, W.Q.; Zeng, D.C.; Wen, L.S. Structural, electronic and magnetic properties of partially inverse spinel CoFe2O4: A first-principles study. *J. Phys. D Appl. Phys.* **2010**, *43*, 445003. [CrossRef]

42. McIntyre, N.S.; Cook, M.G. X-Ray Photoelectron Studies on Some Oxides and Hydroxides of Cobalt, Nickel, and Copper. *Anal. Chem.* **1975**, *47*, 2208–2213. [CrossRef]

43. Yang, J.; Liu, H.; Martens, W.N.; Frost, R.L. Synthesis and Characterization of Cobalt Hydroxide, Cobalt Oxyhydroxide, and Cobalt Oxide Nanodiscs. *J. Phys. Chem. C* **2010**, *114*, 111–119. [CrossRef]

44. Sun, W.; Pan, W.; Wang, F.; Xu, N. Removal of Se(IV) and Se(VI) by MFe_2O_4 nanoparticles from aqueous solution. *Chem. Eng. J.* **2015**, *273*, 353–362. [CrossRef]

45. Bärnighausen, H.; Schiller, G. The Crystal Structure of A-Ce_2O_3. *J. Less-Comm. Met.* **1985**, *110*, 385–390. [CrossRef]

46. Bera, P.; Cámara, A.L.; Hornés, A.; Martínez-Arias, A. Comparative in Situ DRIFTS-MS Study of [12]CO- and [13]CO-TPR on CuO/CeO_2 Catalyst. *J. Phys. Chem. C* **2009**, *113*, 10689–10695. [CrossRef]

47. Martínez-Arias, A.; Gamarra, D.; Hungría, A.B.; Fernández-García, M.; Munuera, G.; Hornés, A.; Bera, P.; Conesa, J.C.; Cámara, A.L. Characterization of Active Sites/Entities and Redox/Catalytic Correlations in Copper-Ceria-Based Catalysts for Preferential Oxidation of CO in H_2-Rich Streams. *Catalysts* **2013**, *3*, 378–400. [CrossRef]

48. Hollins, P. The influence of surface defects on the infrared spectra of adsorbed species. *Surf. Sci. Rep.* **1992**, *16*, 51–94. [CrossRef]

49. Bera, P.; Hornés, A.; Cámara, A.L.; Martínez-Arias, A. DRIFTS-MS studies of preferential oxidation of CO in H_2 rich stream over $(CuO)_{0.7}(CeO_2)_{0.3}$ and $(Cu_{0.9}M_{0.1}O)_{0.7}(CeO_2)_{0.3}$ (M = Co, Zn and Sn) catalysts. *Catal. Today* **2010**, *155*, 184–191. [CrossRef]

50. Martínez-Arias, A.; Fernández-García, M.; Hungría, A.B.; Conesa, J.C.; Munuera, G. Spectroscopic Characterization of Heterogeneity and Redox Effects in Zirconium−Cerium (1:1) Mixed Oxides Prepared by Microemulsion Methods. *J. Phys. Chem. B* **2003**, *107*, 2667–2677. [CrossRef]